Dense cellular segmentation for EM using 2D-3D neural network ensembles

Matthew Guay[1,+,*], **Zeyad Emam**[1,2,+], **Adam Anderson**[1,2], **Maria Aronova**[1], **and Richard Leapman**[1]

[1]National Institute of Biomedical Imaging and Bioengineering, NIH, Bethesda, 20892, USA
[2]University of Maryland, College Park, 20740
[*]matthew.guay@nih.gov
[+]these authors contributed equally to this work

ABSTRACT

Modern electron microscopes produce an unprecedented volume of nanoscale image data. Biologists can build rich 3D structural cell models by densely segmenting cell content within EM images, but manually creating accurate segmentations is infeasible at scale. Our proposed 2D-3D neural network ensembles produce dense cellular segmentations of a gigavoxel EM image with accuracy levels outperforming baselines and approaching laboratory human annotators.

Biomedical researchers use electron microscopy (EM) to image cells, organelles, and their constituents at the nanoscale. The serial block-face scanning electron microscope (SBF-SEM)[1] uses automated serial sectioning techniques to rapidly produce gigavoxel image volumes and beyond. This rapid growth in throughput challenges traditional image analytic workflows for EM, which rely on trained humans to identify salient image features. We study *dense cellular segmentation* problems, which classify each voxel in an image into categories from a detailed schema of cellular and subcellular structures. Structural biologists can use dense cellular segmentations to make rich 3D models of cell structure which yield new insights for biology[2], but applying this method across entire SBF-SEM datasets is infeasible unless analytic bottlenecks are automated.

It is challenging to automate dense segmentation tasks for EM due to the image complexity of biological structures at the nanoscale. An image with little noise and high contrast between features may be accurately segmented with simple thresholding methods, while accurate segmentation of complicated images with multiscale features, noise, and textural content remains an open problem for many biomedical applications. The need for solutions to these problems has driven seminal contributions to image segmentation literature from EM microscopy, including the U-Net[3], 3D U-Net variants[4,5], and newer volumetric segmentation applications[6–10]. We introduce a new 3D biomedical segmentation algorithm based on ensembles of neural networks with separate 2D and 3D prediction modules, building off of existing work in volumetric image segmentation[8,11,12] to solve a dense segmentation task for platelet SBF-SEM datasets. We show that our algorithm outperforms baselines, has comparable image quality to our human annotators, and closely matches human performance on a downstream biological analysis task. We also provide a full segmentation of a gigavoxel platelet image to demonstrate the capabilities of our approach.

Datasets. The datasets used in this study consist of 3D electron microscopy image volumes from two human platelet samples: Subject1 and Subject2. We focus on four datasets: *training data* ($50 \times 800 \times 800$ voxels), *evaluation data* ($24 \times 800 \times 800$ voxels), *test data* ($121 \times 609 \times 400$ voxels), and *annotator comparison data* ($110 \times 602 \times 509$ voxels). The training and eval data are subvolumes taken from Subject1. The test data and annotator comparison data are taken from Subject2. The training and evaluation ground truth labels covered the entirety of their respective images, while the test and annotator comparison labels each covered a single cell contained within their image volumes. The labeling schema divides image content into seven classes, each with an assigned color: `background` (black), `cell` (dark green), `mitochondrion` (fuchsia), `canalicular vessel` (yellow), `alpha granule` (dark blue), `dense granule` (bright red), and `dense granule core` (dark red). Sample images of the data

and human-made ground truth labels can be seen in Figure S1.

Model evaluation. For the main experiment of this study, we compare baseline architectures, our new architecture, and ablations of the new architecture on a dense cellular segmentation task. We conclude that our algorithm outperforms baselines, and that the differentiating features of our final best architecture are responsible for the performance differences. All networks are trained by supervised learning from manually-annotated ground truth labels. The results of this experiment are shown in Figure 1. We consider test performance to be the best indicator of an algorithm's performance as it shows its ability to generalize across different samples. Figure 1 Row 2 compares visualizations of the best 3D segmentation algorithms with ground-truth labels and image data for the test dataset.

We also compare our best algorithm against the segmentations of scientific image annotators, Annotator 1 and Annotator 2, who are laboratory staff trained on annotation tasks but are not biological domain experts. These initial segmentations are currently the first step in producing high-quality dense cellular segmentations, and even before any corrections they require 1-2 work days per cell to create. Results are displayed in Figure 1 Row 3, with further details in Figures S4 and S5. Annotator 1, Annotator 2, and our algorithm each labeled the annotator comparison region from the Subject2 platelet sample. We calculated $\text{MIoU}^{(org)}$ scores pairwise from the three segmentations: 0.571 for Annotator 1 vs. Annotator 2, 0.497 for Annotator 1 vs. Algorithm, and 0.483 for Annotator 2 vs. Algorithm. The confusion matrices in Figure S5 further break down results by organelle class. The statistics indicate that our algorithm disagrees more with either annotator than the annotators do with each other, but none of the labels are consistent everywhere, reflecting the difficulty of dense cellular segmentation even for humans.

We are also interested in understanding how even imperfect segmentations may be useful for downstream analysis tasks. To this end, we computed organelle volume fractions for each organelle within the cell in the annotator comparison dataset. The cell volume fraction of an organelle is equal to the summed voxels of all organelles in a cell, divided by the cell's volume. Biologists can correlate this information with other cell features to better understand variations in the makeup of cellular structures across large samples. The results in Figure 1 Row 4 show that our algorithm tended to underestimate volume fractions relative to the two annotators, but the difference between the algorithm and Annotator 1 is smaller than the difference between Annotator 1 and Annotator 2. The best 3D algorithm improves considerably over the best 2D algorithm. All algorithms detect small regions ignored by humans, but simple postprocessing with small region removal fails to significantly improve quality metrics.

Algorithm design. Inspired by existing work on combining 2D and 3D computations for volumetric data[11,12] we experimented with combinations of 2D and 3D neural modules to trade off between computational efficiency and spatial context. The highest-performing network architecture in this paper, 2D-3D+3x3x3, is a composition of a 2D U-Net-style encoder-decoder and 3D convolutional spatial pyramid, with additional 3x3x3 convolutions at the beginning of convolution blocks in the encoder-decoder. We use same-padded convolution operations throughout, so that 3D operations can be used on anisotropic data windows with small size along the z axis.

Our best algorithms are ensembles that average the per-voxel class probability distributions across several networks. The ensembled networks are identical architectures trained from different random weight initializations. When describing segmentation algorithms, we use Top-k to indicate an ensemble of the best k instances of an architecture. Figure 2 details our best network architecture and illustrates the ensembling process. Figure 1 Row 4 highlights the most notable performance results, and more performance statistics can be found in Table S1. Full algorithm implementation details are in Methods.

In conclusion, we have argued here that dense semantic labeling of 3D EM images for biomedicine is an image analysis method with transformative potential for structural biology. We demonstrated that while challenges exist for both human and algorithmic labelers, automated methods are approaching the performance of trained humans, and may be integrated into annotation software for greatly enhancing the productivity of humans segmenting large datasets. Without question, challenges remain for creating algorithms that are robust to the many types of variation present across research applications. However, SBF-SEM analysis problems are a fertile early ground for this computer vision research, as their large dataset sizes make the entire train-test-deploy cycle of supervised learning viable for accelerating analysis of even individual samples. We believe that the image in Figure **??** showcases this best - after manually segmenting less than 1% of the Subject 1 dataset, we were able to train a segmentation algorithm that produces a high-quality segmentation of the full dataset, a feat that would be impossible with anything

short of an army of human annotators. While gains in accuracy will be realized with future developments, the procedure of training neural network ensembles on a manually annotated portion of a large SBF-SEM dataset is already becoming viable for making dense cellular segmentation a reality.

Online content

Methods, supplementary materials, source data, code, and reproducible examples are available online at https://leapmanlab.github.io/dense-cell.

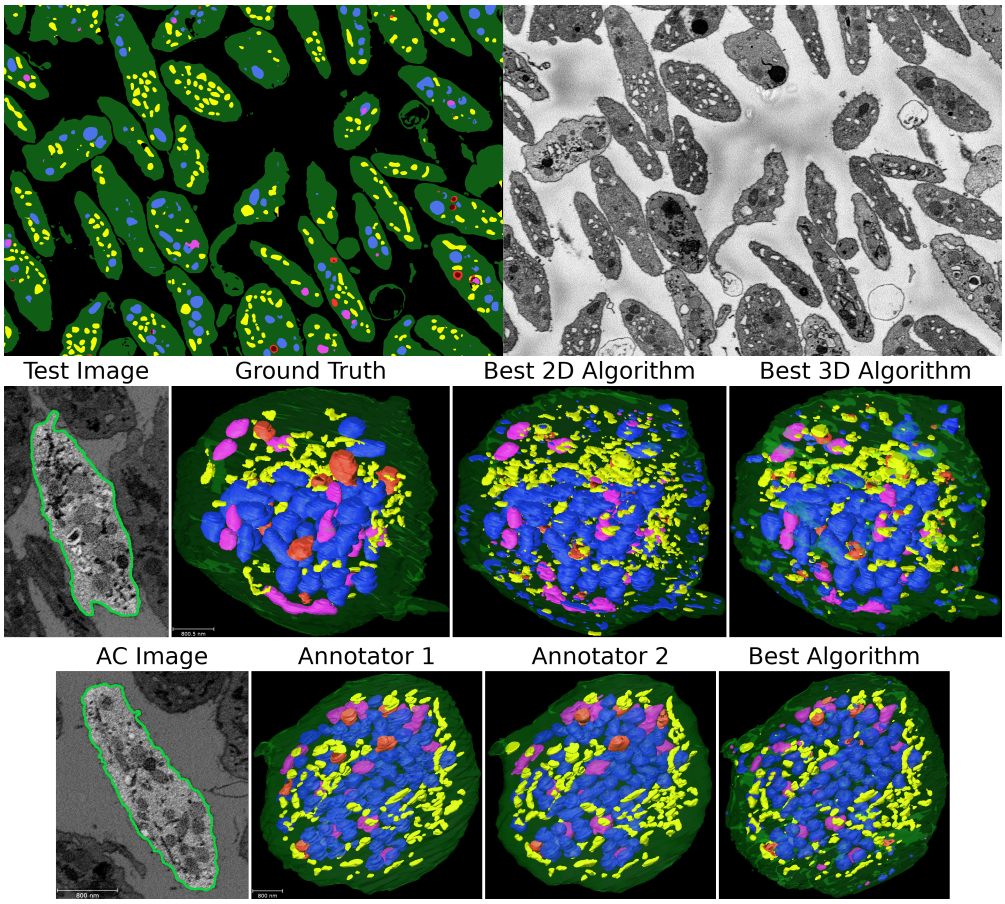

Algorithm	Eval MIoU$^{(org)}$	Test MIoU$^{(org)}$
Top-4 2D-3D+3x3x3	0.595	**0.446**
2D-3D+3x3x3 (10.3M)	0.568	0.417
Original U-Net (31.0M)	0.515	0.334
3D U-Net Thin (2.0M)	0.502	0.280
Deeplab + DRN (40.7M)	0.522	0.130

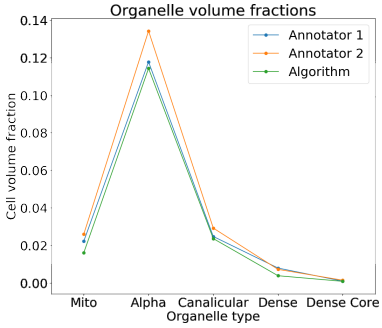

Figure 1. Dense cellular segmentation of platelet cells. (**Row 1**) 2D image of large-scale segmentation of structures in a platelet sample. (**Row 2**) Test dataset comparison between ground-truth labels and the best 2D and 3D algorithms. (**Row 3**) Comparison between two laboratory annotators and the best algorithm on the annotator comparison (AC) dataset. (**Row 4**) Direct and indirect evaluation metrics for segmentation algorithms. *Left*: Segmentation results summary showing mean intersection-over-union across organelle classes (MIoU$^{(org)}$) on evaluation and test data. For a complete table of results, see S1. *Right*: A comparison of organelle volume fractions between two human annotators and our best algorithm on the Annotator Comparison dataset. For each organelle type in a cell, the organelle volume fraction is defined as the volume of all organelles of that type divided by cell volume.

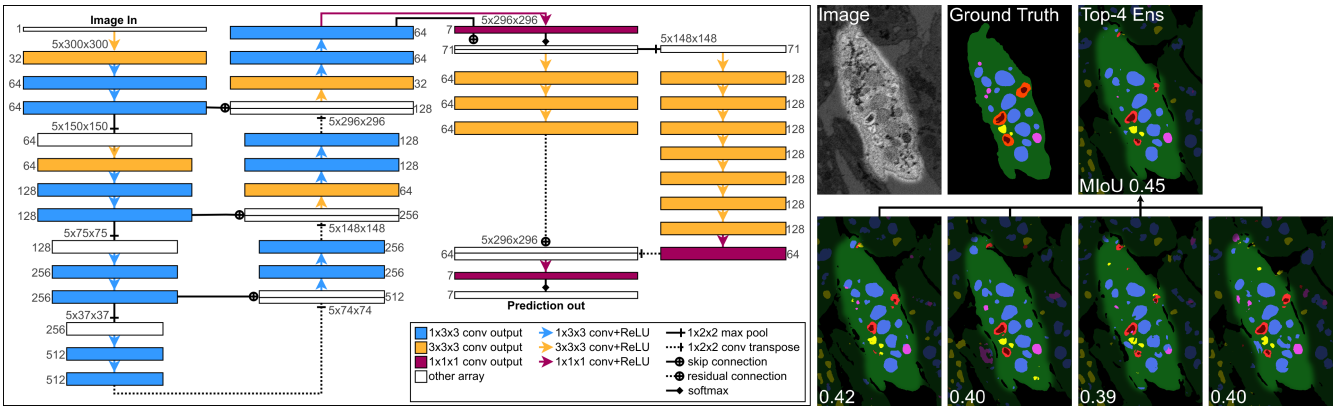

Figure 2. Segmentation algorithm method. (**Left**) Diagram of the 2D-3D+3x3x3 network architecture, the best design tested in this paper. (**Right**) Illustration of initialization-dependent performance of trained segmentation networks, and exploiting it for ensembling. An ensemble of the best 4 trained 2D-3d+3x3x3 network instances improves MIoU$^{(org)}$ by 7.1% over the best single network.

References

1. Denk, W. & Horstmann, H. Serial Block-Face Scanning Electron Microscopy to Reconstruct Three-Dimensional Tissue Nanostructure. *PLoS Biol.* **2**, DOI: 10.1371/journal.pbio.0020329 (2004).

2. Pokrovskaya, I. D. *et al.* 3d ultrastructural analysis of α-granule, dense granule, mitochondria, and canalicular system arrangement in resting human platelets. *Res. Pract. Thromb. Haemostasis* (2019).

3. Ronneberger, O., Fischer, P. & Brox, T. U-Net: Convolutional Networks for Biomedical Image Segmentation. In *LNCS*, vol. 9351, 234–241, DOI: 10.1007/978-3-319-24574-4_28 (2015).

4. Milletari, F., Navab, N. & Ahmadi, S.-A. V-net: Fully convolutional neural networks for volumetric medical image segmentation. In *2016 Fourth International Conference on 3D Vision (3DV)*, 565–571 (IEEE, 2016).

5. Çiçek, Ö., Abdulkadir, A., Lienkamp, S. S., Brox, T. & Ronneberger, O. 3d u-net: learning dense volumetric segmentation from sparse annotation. In *International conference on medical image computing and computer-assisted intervention*, 424–432 (Springer, 2016).

6. Chen, H., Dou, Q., Yu, L., Qin, J. & Heng, P.-A. VoxResNet: Deep voxelwise residual networks for brain segmentation from 3d MR images. *NeuroImage* **170**, 446–455, DOI: 10.1016/j.neuroimage.2017.04.041 (2018).

7. Haft-Javaherian, M. *et al.* Deep convolutional neural networks for segmenting 3d in vivo multiphoton images of vasculature in Alzheimer disease mouse models. *PLoS ONE* **14**, DOI: 10.1371/journal.pone.0213539 (2019).

8. Lee, K., Zlateski, A., Ashwin, V. & Seung, H. S. Recursive Training of 2d-3d Convolutional Networks for Neuronal Boundary Prediction. In Cortes, C., Lawrence, N. D., Lee, D. D., Sugiyama, M. & Garnett, R. (eds.) *Advances in Neural Information Processing Systems 28*, 3573–3581 (Curran Associates, Inc., 2015).

9. Roth, H. R. *et al.* An application of cascaded 3d fully convolutional networks for medical image segmentation. *Comput. Med. Imaging Graph.* **66**, 90–99, DOI: 10.1016/j.compmedimag.2018.03.001 (2018).

10. Fu, H., Xu, Y., Lin, S., Wong, D. W. K. & Liu, J. Deepvessel: Retinal vessel segmentation via deep learning and conditional random field. In *International conference on medical image computing and computer-assisted intervention*, 132–139 (Springer, 2016).

11. Chen, J., Yang, L., Zhang, Y., Alber, M. & Chen, D. Z. Combining fully convolutional and recurrent neural networks for 3d biomedical image segmentation. In *Advances in neural information processing systems*, 3036–3044 (2016).

12. Patravali, J., Jain, S. & Chilamkurthy, S. 2d-3d fully convolutional neural networks for cardiac mr segmentation. In *International Workshop on Statistical Atlases and Computational Models of the Heart*, 130–139 (Springer, 2017).

13. Stalling, D., Westerhoff, M., Hege, H.-C. *et al.* Amira: A highly interactive system for visual data analysis. *The visualization handbook* **38**, 749–67 (2005).

14. Krogh, A. & Vedelsby, J. Neural network ensembles, cross validation, and active learning. In *Advances in neural information processing systems*, 231–238 (1995).

15. Guay, M., Emam, Z., Anderson, A. & Leapman, R. Designing deep neural networks to automate segmentation for serial block-face electron microscopy. In *2018 IEEE 15th International Symposium on Biomedical Imaging (ISBI 2018)*, 405–408 (IEEE, 2018).

16. Chen, L.-C., Papandreou, G., Kokkinos, I., Murphy, K. & Yuille, A. L. Deeplab: Semantic image segmentation with deep convolutional nets, atrous convolution, and fully connected crfs. *IEEE transactions on pattern analysis machine intelligence* **40**, 834–848 (2017).

17. Chen, L.-C., Papandreou, G., Schroff, F. & Adam, H. Rethinking atrous convolution for semantic image segmentation. *arXiv preprint arXiv:1706.05587* (2017).

18. He, K., Zhang, X., Ren, S. & Sun, J. Deep Residual Learning for Image Recognition. In *2016 IEEE Conference on Computer Vision and Pattern Recognition (CVPR)*, 770–778, DOI: 10.1109/CVPR.2016.90 (2016). ISSN: 1063-6919.

Methods

SBF-SEM image volumes were obtained from identically-prepared platelet samples from two humans. Lab members manually segmented portions of each volume into seven classes to analyze the structure of the platelets. The labels were used for the supervised training of candidate network architectures, as well as baseline comparisons. We trained multiple instances of candidate architectures, each with different random initializations. The best-performing instances were ensembled together to produce the final segmentation algorithms used in this paper.

Data collection

This study used datasets prepared from two human platelet samples as part of a collaborative effort between the National Institute of Biomedical Imaging and Bioengineering (NIBIB), NIH and the University of Arkansas for Medical Sciences. The platelet samples were imaged using a Zeiss 3View SBF-SEM. The Subject 1 dataset is a $250 \times 2000 \times 2000$ voxel image with a lateral resolution of 10 nm and an axial resolution of 50 nm, from a sample volume with dimensions $12.5 \times 20 \times 20 \mu\text{m}^3$. The Subject 2 dataset is a $239 \times 2000 \times 2000$ voxel image produced by the same imaging protocol, with the same resolution and coming from a sample volume with the same dimensions. We assembled labeled datasets from manually-segmented regions of the platelet datasets. Lab members created initial manual segmentations using Amira[13]. For the training, evaluation, and test dataset, segmentations were reviewed by subject experts and corrected. The training image was a $50 \times 800 \times 800$ subvolume of the Subject 1 dataset spanning the region $81 \leq z \leq 130$, $1073 \leq y \leq 1872$, $620 \leq x \leq 1419$ in 0-indexed notation. The evaluation image was a $24 \times 800 \times 800$ subvolume of the Subject 1 dataset spanning the region $100 \leq z \leq 123$, $200 \leq y \leq 999$, $620 \leq x \leq 1419$. The test image was a $121 \times 609 \times 400$ subvolume of the Subject 2 dataset spanning the region $0 \leq z \leq 120$, $460 \leq y \leq 1068$, $308 \leq x \leq 707$. The annotator comparison image was a $110 \times 602 \times 509$ subvolume of the Subject 2 dataset spanning the region $116 \leq z \leq 225$, $638 \leq y \leq 1239$, $966 \leq x \leq 1474$. The training and evaluation labels covered the entirety of their respective images, while the test and annotator comparison labels covered a single cell contained within their image volumes. The labeling schema divides image content into seven classes: `background` (0), `cell` (1), `mitochondrion` (2), `canalicular vessel` (3), `alpha granule` (4), `dense granule` (5), and `dense granule core` (6).

Neural architectures and ensembling

The Subject 1 and Subject 2 datasets were binned by 2 in x and y, and aligned. For each of the training, evaluation, and testing procedures, the respective image subvolumes were normalized to have mean 0 and standard deviation 1 before further processing.

The highest-performing network architecture in this paper, 2D-3D+3x3x3, is a composition of a 2D U-net-style encoder-decoder and 3D convolutional spatial pyramid, with additional 3x3x3 convolutions at the beginning of convolution blocks in the encoder-decoder. All convolutions are zero-padded to preserve array shape throughout the network, allowing deep architectures to operate on data windows with small z-dimension. A ReLU activation follows each convolution. All convolution and transposed convolutions use bias terms. The architecture is fully specified as a diagram in Figure 2. Additionally, several baseline comparison networks and three 2D-3D+3x3x3 ablation networks were also tested in this paper and are described in the Validation and Performance Metrics section.

To build a 2D-3D network, one can adapt a 2D U-net-style encoder-decoder module to work on 3D data by recasting 2D 3x3 convolutions as 1x3x3 convolutions, and 2D 2x2 max-pooling and transposed convolution layers as 1x2x2 equivalents. In this way, a 3D input volume can be processed as a sequence of independent 2D regions in a single computation graph, and the 2D and 3D modules can be jointly trained end-to-end. Intermediate 2D class predictions $\hat{x}_{2D}$ are formed from the 2D module output, and the 2D output and class predictions are concatenated along the feature axis to form an input to a 3D spatial pyramid module. The 3D module applies a 1x2x2 max pool to its input to form a two-level spatial pyramid with scales 0 (input) and 1 (pooled). The pyramid elements separately pass

through convolution blocks, and the scale 1 block output is upsampled and added to the scale 0 block output with a residual connection to form the module output. 3D class predictions $\hat{x}_{3D}$ are formed from the 3D module output, and the final segmentation output $\hat{\ell}$ of the algorithm is a voxelwise argmax of the 3D class predictions. To build a 2D-3D+3x3x3 network, we inserted 3x3x3 convolution layers at the beginning of the first two convolution blocks in the 2D encoder and the last two convolution blocks in the 2D decoder.

Given a collection of networks' 3D class predictions, one can form an ensemble prediction by computing a voxelwise average of the predictions and computing a segmentation from that. Ensembling high-quality but non-identical predictions can produce better predictions[14], and there is reason to think that more sophisticated ensembles could be constructed from collections of diverse neural architectures[15], but in this paper we use a simple source of differing predictions to boost performance: ensembles of identical architectures trained from different random initializations. The sources of randomness in the training procedure are examined more thoroughly in the Validation and Performance Metrics section, but in our experiments this variation produced a small number of high-performing network instances per architecture with partially-uncorrelated errors.

Network training

Assume a network predicting classes $C = \{0, \ldots, 6\}$ for each voxel in a shape-(o_z, o_x, o_y) data window Ω containing $N = o_z o_x o_y$ voxels $\{v_i\}_{i=1}^{N}$. The ground-truth segmentation of this region is a shape-(o_z, o_x, o_y) array ℓ such that $\ell(v) \in C$ is the ground-truth label for voxel v. A network output prediction is a shape-$(7, o_z, o_x, o_y)$ array $\hat{x}$ such that $x_v \triangleq \hat{x}(:, v)$ is a probability distribution over possible class labels for voxel v. The corresponding segmentation $\hat{\ell}$ is the per-voxel arg max of $\hat{x}$. Inversely, from ℓ one may construct a shape-$(7, o_z, o_x, o_y)$ per-voxel probability distribution x such that $x_v(i) = 1$ if $i = \ell(v)$ and 0 if not, which is useful during training.

We trained our networks as a series of experiments, with each experiment training and evaluating 1 or more instances of a fixed network architecture. Instances within an experiment varied only in the random number generator (RNG) seed used to control trainable variable initialization and training data presentation order. In addition to the main 2D-3D+3x3x3 architecture, there were three ablation experiments - No 3x3x3 Convs, No Multi-Loss, No 3D Pyramid - and five baseline experiments - Original U-Net, 3D U-Net Thin, 3D U-Net Thick, Deeplab + DRN, and Deeplab + ResNet101. Instances were trained and ranked by evaluation dataset MIoU. Experiments tracked evaluation MIoU for each instance at each evaluation point throughout training, and saved the final weight checkpoint as well as the checkpoint with highest eval MIoU. In this work we report eval MIoU checkpoints for each instance. The 2D-3D+3x3x3 experiment and its ablations trained 26 instances for 40 epochs with minibatch size 1 (33k steps). The Original U-Net experiment trained 500 instances for 100 epochs with minibatch size 1 (180k steps). The 3D U-Net Thin experiment trained 26 instances for 100 epochs with minibatch size 1 (29k steps), and the 3D U-Net Thick experiment trained 26 instances for 100 epochs with minibatch size 1 (30k steps). The Deeplab + DRN and Deeplab + ResNet101 experiments trained 1 instance each for 200 epochs with minibatch size 4 (360k steps). Due to poor performance and slow training times of the Deeplab models, we deemed it unnecessary to train further instances. Networks were trained on NVIDIA GTX 1080 and NVIDIA Tesla P100 GPUs.

This subsection details the training of the 2D-3D+3x3x3 network. Baseline and ablation networks were trained identically except as noted in Validation and Performance Metrics. All trainable variables were initialized from Xavier uniform distributions. Each instance was trained for 40 epochs on shape-$(5, 300, 300)$ windows extracted from the training volume, and output a shape-$(7, 5, 296, 296)$ class prediction array. The number of windows in each epoch was determined by a window spacing parameter which determined the distance along each axis between the top-back-left corners of each window, here $(2, 100, 100)$, resulting in 828 windows per epoch. An early stopping criterion halted the training of any network that failed to reach an MIoU of 0.3 after 10 epochs.

Networks were trained using a regularized, weighted sum of cross-entropy functions. The network has a set Θ trainable variables divided into four subsets: Θ_{2D} for variables in the 2D encoder-decoder module, Θ_{3D} for variables in the 3D spatial pyramid module, the single 1x1x1 convolution variable $\{\theta_{2DP}\}$ which produces intermediate 2D class predictions $\hat{x}_{2D}$ from the encoder-decoder's 64 output features, and the single 1x1x1 convolution variable $\{\theta_{3DP}\}$ which produces the final 3D class predictions $\hat{x}_{3D}$ from the spatial pyramid's 64 output features. Predictions

are compared against ground-truth labels as

$$L(x,\hat{x}_{3D},\hat{x}_{2D};\Theta) = \frac{1}{N}\sum_{i=1}^{N}\left[\mathcal{W}\otimes\mathcal{H}\left(x,\hat{x}_{3D}\right)\right]_i + \frac{c_{2D}}{N}\sum_{i=1}^{N}\left[\mathcal{W}\otimes\mathcal{H}\left(x,\hat{x}_{2D}\right)\right] + \lambda_{2D}\sum_{\theta\in\Theta_{2D}}\|\theta\|_2^2 + \lambda_{3D}\sum_{\theta\in\Theta_{3D}}\|\theta\|_2^2 + \lambda_P\left(\|\theta_{2DP}\|_2^2 + \|\theta_{3DP}\|_2^2\right), \quad (1)$$

where $\lambda_{2D} = 1\times10^{-4.7}$ and $\lambda_{3D} = 1\times10^{-5}$ are L^2 regularization hyperparameters for the variables in Θ_{2D} and Θ_{3D}, $\lambda_P = 1\times10^{-9}$ is an L^2 regularization hyperparameter for the predictor variables θ_{2DP} and θ_{3DP}, and $c_{2D} = 0.33$ is a constant that weights the importance of the intermediate 2D class predictions in the loss function. $\mathcal{H}(x,\hat{x})$ is the voxelwise cross-entropy function, i.e.,

$$\mathcal{H}(x,\hat{x})_v \triangleq H(x_v,\hat{x}_v) \triangleq -\sum_{j=1}^{7} x_v(j)\log\left[\hat{x}_v(j)\right] = -x_v(\ell_v)\log\left[\hat{x}_v(\ell_v)\right].$$

$\mathcal{W}$ is a shape-$(5,296,296)$ array of weights; its Kronecker product with $\mathcal{H}$ produces a relative weighting of the cross-entropy error per voxel. This weighting strategy is based generally on the approach in (Ronneberger et al., 2015)[3]:

$$\mathcal{W} \triangleq w + \mathcal{W}_{cb} + \mathcal{W}_{ep}.$$

The initial $w = 0.01$ is a constant that sets a floor for the minimum weight value, $\mathcal{W}_{cb}$ is a class-balancing term such that $\mathcal{W}_{cb,i} \propto 1/N_i$, where N_i is the number of occurrences in the training data of ℓ_i, rescaled so that $\max\mathcal{W}_{cb} = 1$. $\mathcal{W}_{ep}$ is an edge-preserving term that upweights voxels near boundaries between image objects and within small 2D cross-sections. In (Ronneberger et al., 2015) this is computed using morphological operations. We used a sum of scaled, thresholded diffusion operations to approximate this strategy in a manner that requires no morphological information. $\mathcal{W}_{ep}$ is built up as a rectified sum of four terms:

$$\mathcal{W}_{ep} \triangleq R_\alpha\left(\mathcal{W}_{bkgd\to cell} + \mathcal{W}_{cell\to bkgd} + \mathcal{W}_{cell\to org} + \mathcal{W}_{org\to cell}\right),$$

where $R_\alpha(W) = \mathrm{ReLU}(W-\alpha)\cdot\frac{\max W}{\max W-a}$. For each term, we choose two disjoint subsets C_{source} and C_{target} of the classes C. Let ℓ_{source} be the binary image such that $\ell_{source}(v) = 1$ if $\ell(v)\in C_{source}$ and $\ell_{source}(v) = 0$ otherwise. Define

$$M_{source}(c,\sigma) \triangleq c\cdot\ell_{source} * k_\sigma,$$

where $*$ denotes convolution and k_σ is a Gaussian diffusion kernel with standard deviation σ. Then, $\mathcal{W}_{source\to target}(v) = \mathcal{M}_{source}(v)$ if $\ell(v)\in C_{target}$, and is 0 otherwise. The terms in the $\mathcal{W}_{ep}$ array used in this paper were computed using class subsets $bkgd = \{0\}$, $cell = \{1\}$, and $org = \{2,3,4,5,6\}$, $\alpha = 0.25$, $c = 0.882$, and $\sigma = 6$. The error weighting array used in this paper and the code used to generate it are available with the rest of the platelet dataset at `leapmanlab.github.io/dense-cell`. See Figure S7 for a visualization of the error weighting array. $\mathcal{W}_{cb}$ is calculated all at once across the entire 3D training volume, while $\mathcal{W}_{ep}$ is calculated independently per each 2D z-slice of the training volume.

We employed data augmentation to partially compensate for the limited available training data. Augmentations were random reflections along each axis, random shifts in brightness ($\pm12\%$) and contrast ($\pm20\%$), and elastic deformation as in (Ronneberger et al., 2015). For elastic deformation, each 800x800 $x-y$ plane in the shape-$(50,800,800)$ training data and label arrays was displaced according to a shape-$(800,800,2)$ array of 2D random pixel displacement vectors, generated by bilinearly upsampling a shape-$(20,20,2)$ array of iid Gaussian random variables with mean 20 and standard deviation 0.6. During each epoch of training, a single displacement map was created and applied to the entire training volume before creating the epoch's batch of input and output windows. Training used the ADAM optimizer with learning rate 1×10^{-3}, $\beta_1 = 1-1\times10^{-1.5}$, $\beta_2 = 1-1\times10^{-2.1}$, and $\varepsilon = 1\times10^{-7}$. Training also used learning rate decay with an exponential decay rate of 0.75 every $1\times10^{3.4}$ training iterations.

Validation and performance metrics

The performance metric used in this work is mean intersection-over-union (MIoU) between ground-truth image segmentation ℓ's 7 labeled sets $\{L_j = v \in \Omega \,|\, \ell(v) = j\}_{j \in C}$ and predicted segmentation's $\hat{\ell}$ labeled sets $\{\hat{L}_j = v \in \Omega \,|\, \hat{\ell}(v) = j\}_{j \in C}$. Given two sets A and B,

$$\mathrm{IoU}(A,B) = \frac{|A \cap B|}{|A \cup B|}.$$

Then for segmentations ℓ and $\hat{\ell}$ with their corresponding labeled sets,

$$\mathrm{MIoU}(\ell,\hat{\ell}) = \frac{1}{7}\sum_{j \in C} \mathrm{IoU}(L_j,\hat{L}_j).$$

More generally, for a subset of labels $D \subseteq C$, one can compute the MIoU over D, or $\mathrm{MIoU}^{(D)}$, as

$$\mathrm{MIoU}^{(D)}(\ell,\hat{\ell}) = \frac{1}{|D|}\sum_{j \in D} \mathrm{IoU}(L_j,\hat{L}_j).$$

Here we are concerned with MIoUs over two sets of labels: $\mathrm{MIoU}^{(all)}$ over the set of all 7 class labels, and $\mathrm{MIoU}^{(org)}$ over the set of 5 organelle labels 2-7. Our network validation metrics were $\mathrm{MIoU}^{(all)}$ and $\mathrm{MIoU}^{(org)}$ on the evaluation dataset, and $\mathrm{MIoU}^{(org)}$ on the test dataset. Test data uses $\mathrm{MIoU}^{(org)}$ because the labeled region is a single cell among several unlabeled ones, and restricting validation to the labeled region invalidates MIoU stats for the background and cell classes (0 and 1). We include eval $\mathrm{MIoU}^{(org)}$ to quantify how performance drops between a region taken from the physical sample used to generate the training data, and a new physical sample of the same tissue system.

Using this procedure, the performance of the 2D-3D+3x3x3 network was compared against three ablations and five baseline networks. The three ablations each tested one of three features that distinguish the 2D-3D+3x3x3 network in this paper from similar baselines. The first, 2D+3x3x3 No 3x3x3 Convs, replaces the 3x3x3 convolutions in the net's encoder-decoder module with 1x3x3 convolutions that are otherwise identical. With this ablation, the network's encoder-decoder loses any fully-3D layers. The second, 2D+3x3x3 No Multi-Loss, modifies the loss function in Equation (1) by removing the term involving $\hat{x}_{2D}$ but otherwise leaving the architecture and training procedure unchanged. This ablation tests whether it is important to have auxiliary accuracy loss terms during training. The third ablation, 2D-3D+3x3x3 No 3D Pyramid, removes the 3D spatial pyramid module and 3D class predictor module from the network architecture, so that $\hat{x}_{2D}$ is the network's output. Correspondingly, the loss term involving $\hat{x}_{3D}$ is removed from Equation (1).

We implemented five baseline networks by adapting common models in the literature to our platelet segmentation problem. Three of these were 2D - The original U-Net[3] as well as two Deeplab variants[16,17] using a deep residual network (DRN) backbone and a ResNet101 backbone[18], minimally modified to output 7 class predictions. The original U-Net used $(572,572)$ input windows and $(388,388)$ output windows, while the Deeplab variants used $(572,572)$ input and output windows. The two 3D networks were fully-3D U-Net variants adapted on the 3D U-Net in (Çiçek et al., 2016)[5] - 3D U-Net Thin and 3D U-Net Thick. The variants used same-padding, had three convolutions per convolution block, and two pooling operations in the encoder for convolution blocks at three spatial scales. The 3D U-Net Thin network used $(5,300,300)$ input windows and $(5,296,296)$ output windows, and pooling and upsampling operations did not affect the z spatial axis. The 3D U-Net Thick network used $(16,180,180)$ input windows and $(16,180,180)$ output windows, and pooled and upsampled along all three spatial axes.

To determine whether one architecture is superior to another, trained instances are compared with each other. However, sources of randomness in the training process induce a distribution of final performance metric scores across trained instances of an architecture, so that a single sample per architecture may be insufficient to determine which is better. While expensive, a collection of instances can be trained and evaluated to empirically approximate the performance distribution for each architecture. In this way, better inferences may be made about architecture design choices. Figure S6 shows the empirical performance distributions for the 26 trials of the 2D-3D+3x3x3 architecture and its three ablations, as well as the 26 trials of the 3D U-Net and 500 trials of the 2D Original U-Net.

A final point of comparison was drawn between the top algorithm's performance and the initial work of laboratory scientific image annotators, Annotator 1 and Annotator 2. The three sources each labeled the annotator comparison region from the Subject 2 platelet sample. Pairwise $\text{MIoU}^{(org)}$ scores and organelle confusion matrices were calculated to compare the level of disagreement between two human labelings and between humans and the algorithm. We also computed organelle volume fractions for each segmentation to compare performance in segmentation applications to downstream analysis tasks. The cell volume fraction of an organelle is equal to the summed voxels of all organelles in a cell, divided by the cell's volume. To compute this quantity for each organelle, the number of voxels for each organelle label is divided by the number of voxels in the cell. For the algorithmic result, since the semantic segmentation map does not distinguish between separate cells in the field of view, a mask for the single annotator comparison dataset cell was approximated as all non-background-labeled voxels in a small region around the Annotator 1 cell mask.

Supplementary Material

Additional segmentation visualizations

In addition to the renderings in the main paper, we produced 3D renderings of segmentation results for the evaluation dataset, as shown in Figure S2, showing results for all organelles together as well as separately for the ground-truth labels, as well as the best 2D and 3D segmentation algorithms. Similarly, Figure S4 shows renderings per each organelle class for Annotator 1, Annotator 2, and our best algorithm on the annotator comparison dataset. Finally, Figure S3 shows 2D images of segmentations for each of the 14 algorithms tested in this paper, which are also detailed in Table S1.

Ablation analysis and initialization-dependent performance

Our ablation analysis procedure, described in the **Validation and performance metrics** subsection of **Methods** confirms our conjectures about the importance of 3D context input to the network, and the importance of 3x3x3 convolutions over 1x3x3 convolutions for generalization performance. The latter do not capture correlations along the z spatial dimension, likely contributing to their poorer performance. Ablation analysis also indicates that removing either the multi-loss training setup or the 3D spatial pyramid module from the 2D-3D+3x3x3 architecture carries significant performance penalties. Removing either the 3x3x3 convolution layers or the 3D spatial pyramid on their own had a small effect on performance compared with removing the 2D loss term from the multi-loss objective function. Summary statistics demonstrating these results can be seen in Table S1(a), but these statistics only tell part of the story. Especially when effect sizes are small, looking at a single trained instance of each architecture may not be enough to determine relative performance between architecture candidates. To get a better idea of the effects of different architecture choices, we must deal with the initialization-dependent performance of these segmentation networks.

In Figure S6 we experiment with various weight initialization random seeds to determine the robustness of various models to the weight initialization scheme. In order to determine whether one architecture choice is superior to another, the outputs of different trained networks are compared with each other. However, sources of randomness in the training process (initialization of trainable weights from a Xavier uniform distribution, and the random presentation order of training data elements) induce a distribution of final performance metric scores. These scores are random variables, and a single sample per architecture may be insufficient to determine which is better. By empirically approximating the distribution for each architecture, better inferences may be made about architecture design choices. For this figure, multiple instances of the same architecture (26 for 2D-3D and fully-3D nets, 500 for the U-Net) were trained under identical conditions, varying only random number generation seeds. The resulting distributions support the conclusions that 2D-3D networks outperform their 2D and fully-3D counterparts, as well as the conclusions drawn from the ablation studies. They also reveal a curious phenomenon that may be a topic for future study - the seemingly bimodal performance of 2D-3D architectures, wherein some fraction of trained instances perform markedly worse than others with an apparent performance gap between peaks. Whether this is a real phenomenon or an artifact of having an insufficient number of samples could be determined with a followup study.

DeepVess baseline comparison

In addition to the baseline models discussed in the main text, we have also tried using the DeepVess model from (Haft-Javaherian et al., 2019)[7] on our data. However, DeepVess performed poorly, and learned to assign a single class (background) to the entire output patch. We believe there may be two reasons behind DeepVess' poor performance: (1) Unlike U-Net and Deeplab networks, the DeepVess network is designed with very small input patches in mind; small patches do not contain enough context for the network to distinguish between objects. (2) DeepVess' last layer consists of a fully-connected operation with a single hidden layer containing 1024 neurons, therefore any attempt to input significantly larger patches would require increasing the number of neurons in the last layer, but fully-connected layers do not scale well and the network quickly outgrows GPU memory.

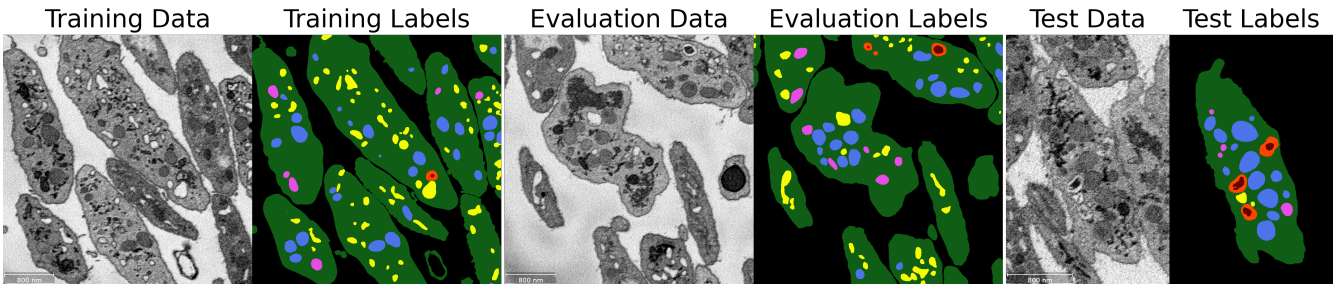

Figure S1. Dataset visualization. Sample images of the datasets used in this study.

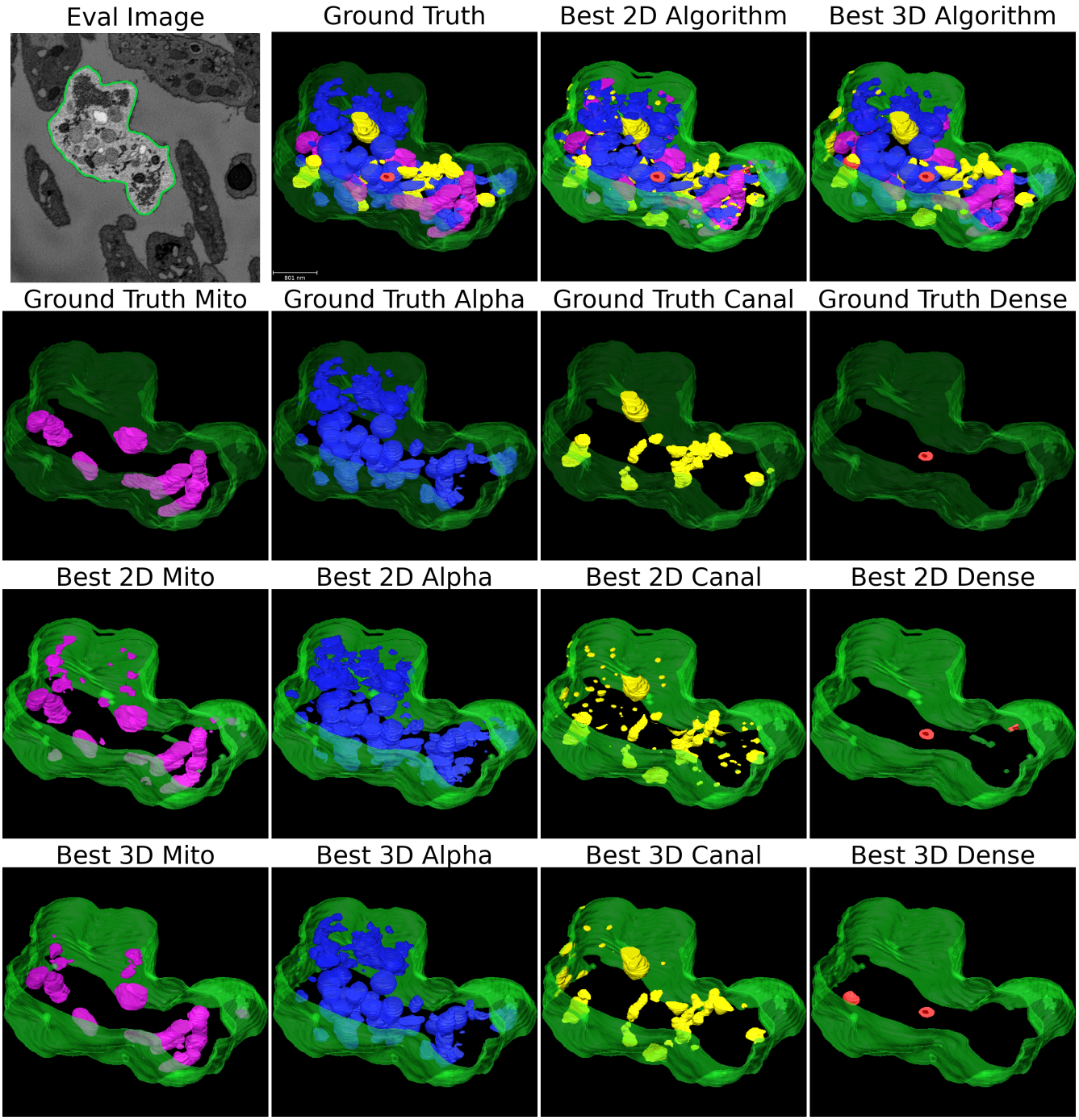

Figure S2. 3D eval segmentation renderings. (**Row 1**) Summary visualizations highlighting the cell featured in the renderings, as well as ground truth and best 2D and 3D segmentations of the cell and all its organelles. (**Row 2**) Renderings for individual organelle types in the ground truth segmentation: Mito for mitochondria, Alpha for alpha granules, Canal for canalicular vessels, and Dense for dense granules. (**Row 3**) Renderings for individual organelle types in the best 2D algorithm's segmentation. (**Row 4**) Renderings for individual organelle types in the best 3D algorithm's segmentation.

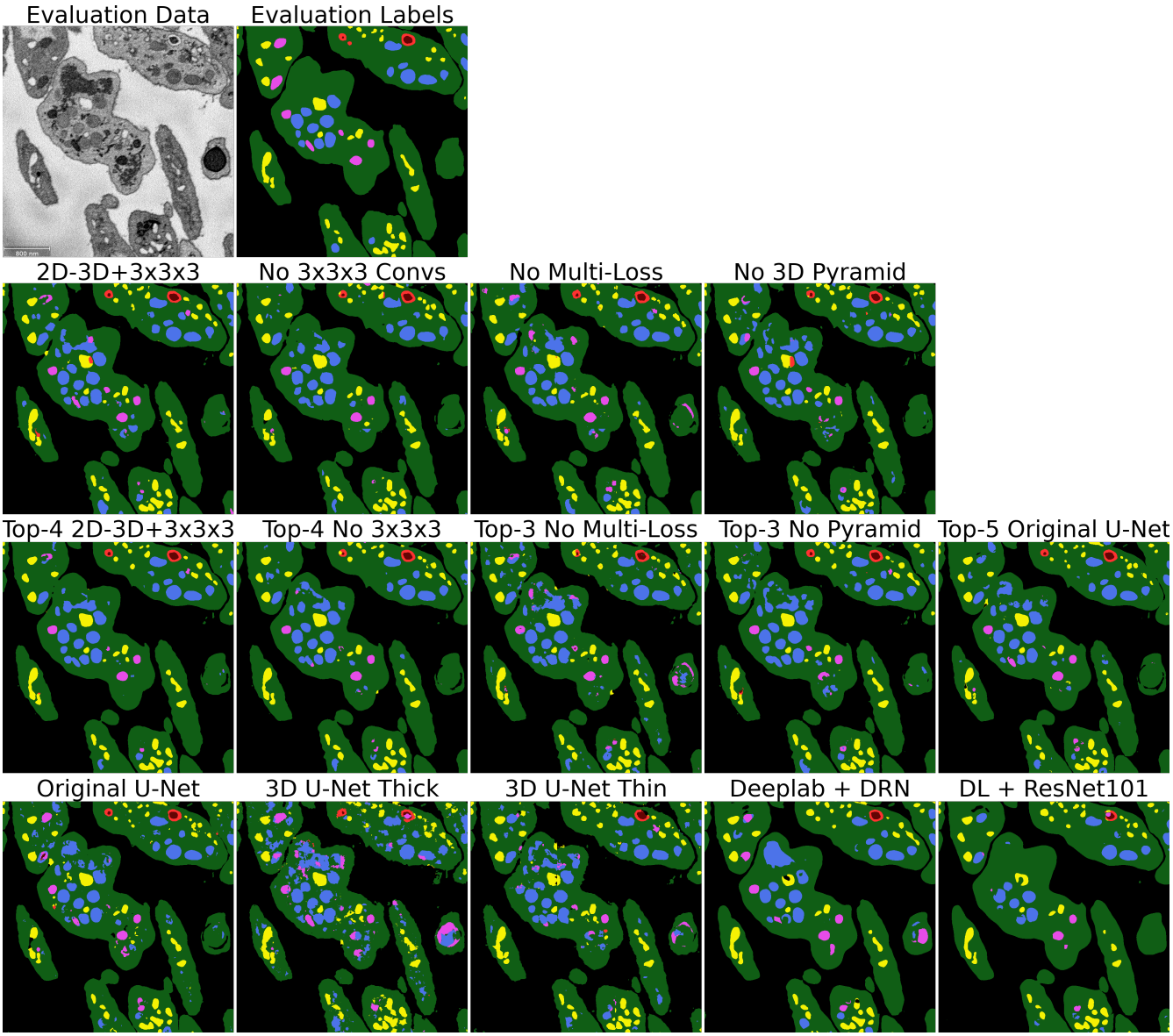

Figure S3. 2D comparison of all algorithm results. This figure compares the results of all 14 segmentation algorithms tested in this paper with ground-truth labels for the $z = 4$ slice of the evaluation dataset. (**Row 1**) Image of the $z = 4$ slice of the evaluation dataset and corresponding ground-truth labels. (**Row 2**) Segmentation results for the novel 2D-3D+3x3x3 network and its three ablations. (**Row 3**) Segmentation results for the five network ensembles tested in this paper. (**Row 4**) Segmentation results for the five baseline networks tested in this paper in comparison with our new 2D-3D+3x3x3 network.

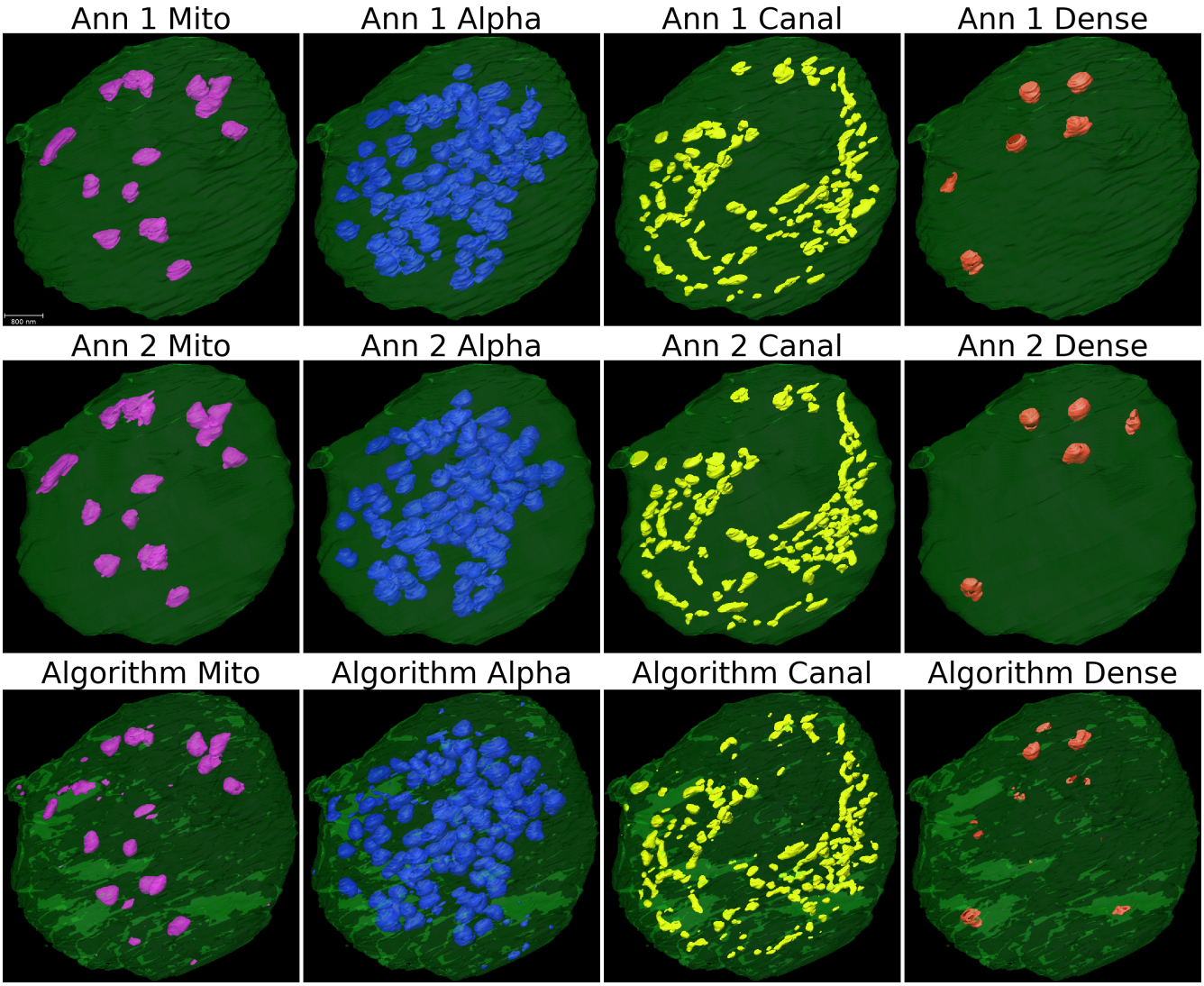

Figure S4. Detailed annotator comparison 3D renderings. This figure supplements Row 4 of Figure 1 by showing renderings of individual organelle types - Mito for mitochondria, Alpha for alpha granules, Canal for canalicular vessels, Dense for dense granules - from the Annotator 1, Annotator 2, and best Algorithm (Top-4 2D-3D+3x3x3) segmentations. (**Row 1**) Annotator 1 segmentation results. (**Row 2**) Annotator 2 segmentation results. (**Row 3**) Algorithm segmentation results.

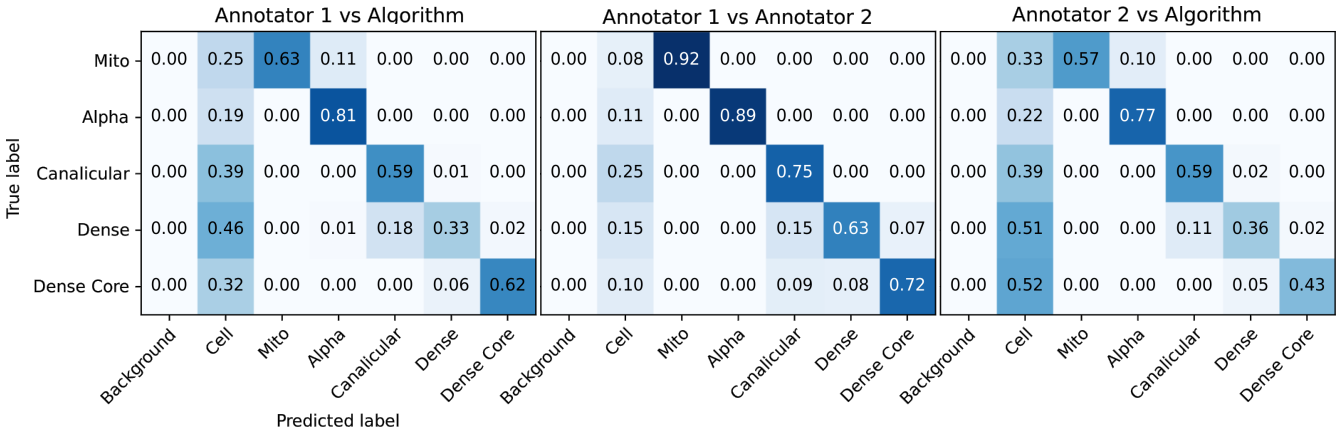

Figure S5. Annotator comparison confusion matrices. Here, we show further statistical details comparing the performance of human and algorithmic annotation strategies. Confusion matrices comparing organelle labelings pairwise between the two annotators and the algorithm. The confusion matrices give a more detailed performance breakdown of the three $\text{MIoU}^{(org)}$ scores obtained for each comparison: 0.571 for Annotator 1 vs. Annotator 2, 0.497 for Annotator 1 vs Algorithm, and 0.483 for Annotator 2 vs Algorithm.

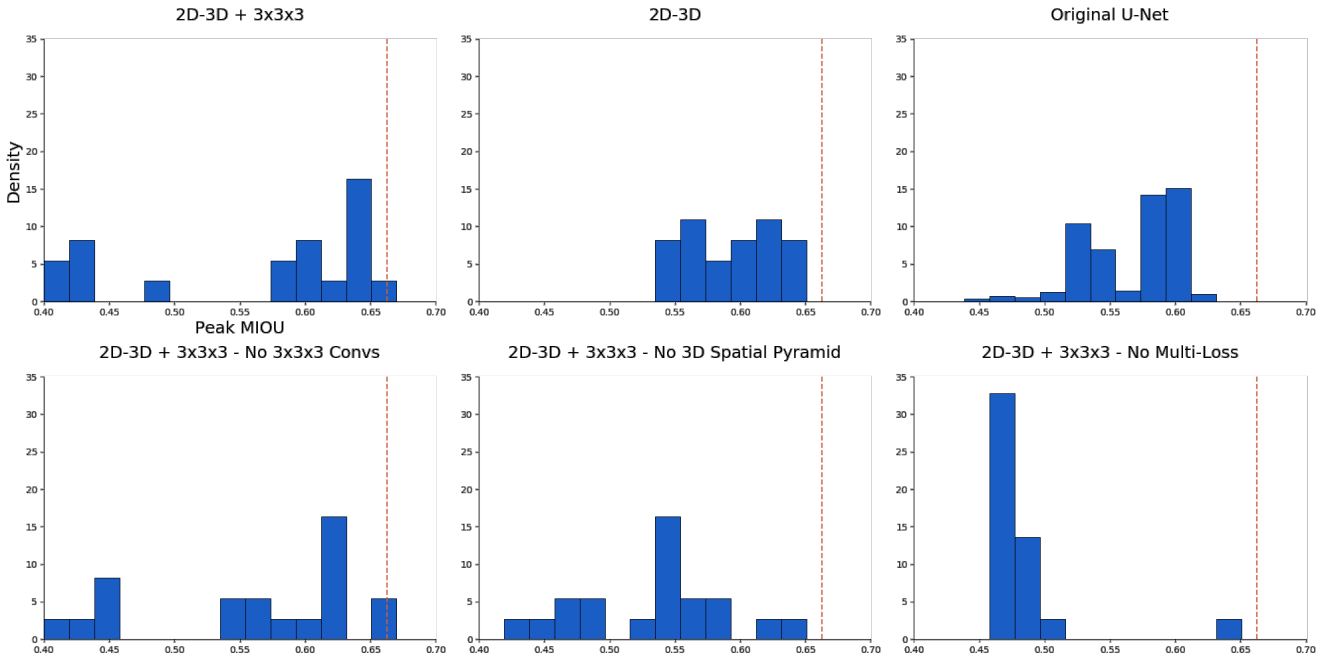

Figure S6. Making better architecture design decisions. This figure shows normalized histograms of peak $\text{MIoU}^{(all)}$ on the evaluation dataset for each of the architectures examined in this paper. In order to determine whether one architecture choice is superior to another, the outputs of different trained networks are compared with each other. However, sources of randomness in the training process (initialization of trainable weights from a Xavier uniform distribution, and the random presentation order of training data elements) induce a distribution of final performance metric scores. These scores are random variables, and a single sample per architecture may be insufficient to determine which is better. By empirically approximating the distribution for each architecture, better inferences may be made about architecture design choices. For this figure, multiple instances of the same architecture (26 for 2D-3D nets, 500 for the U-Net) were trained under identical conditions, varying only random number generation seeds. The resulting distributions support the conclusions that 2D-3D networks outperform the 2D U-Net and that multi-loss training is necessary for 2D-3D architectures.

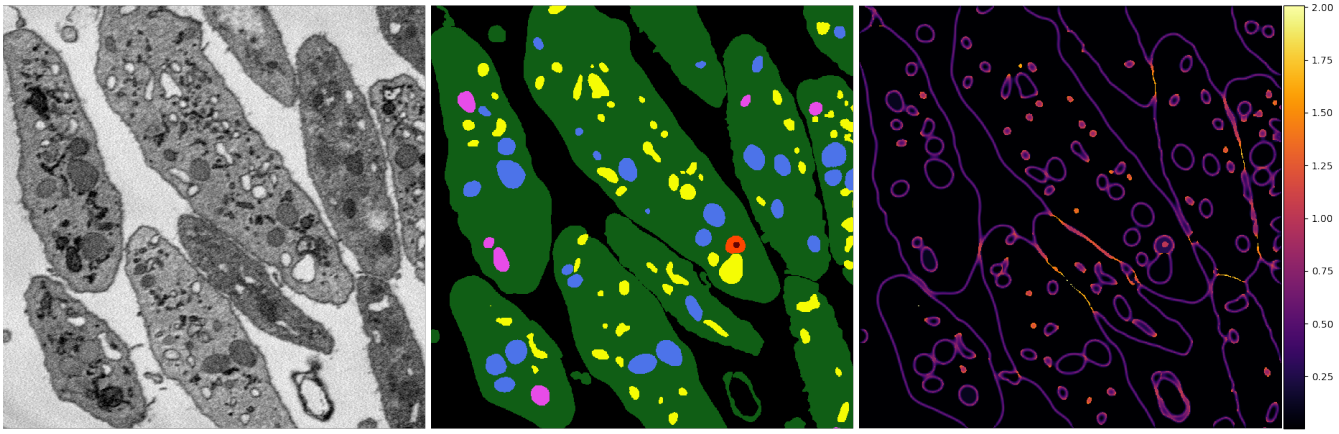

Figure S7. Visualization of the error weighting array used for network training in this paper, compared with the corresponding image region and ground-truth labels. The error weighting $\mathcal{W}$ array is the sum of three terms $w + \mathcal{W}_{cb} + \mathcal{W}_{ep}$, where $w = 0.01$ is a weight floor, $\mathcal{W}_{cb}$ is a class frequency balancing array, and $\mathcal{W}_{ep}$ is an edge preserving array. $\mathcal{W}_{cb}$ assigns a weight to each voxel that is inversely proportional to the frequency with which that voxel's label appears in the dataset. The weights are scaled so that the largest weight, corresponding to the rarest label class, is equal to 1. $\mathcal{W}_{ep}$ enforces accurate classification of edges, especially in regions where two objects come close to each other in the data, as well as regions with small 2D cross sections, using a sum of thresholded diffusion operations. The sum of these three terms is shown in the right-most graphic here.

	Eval MIoU$^{(all)}$	Eval MIoU$^{(org)}$	Test MIoU$^{(org)}$
Top-4 2D-3D+3x3x3	0.686	0.595	**0.446**
Top-5 No 3x3x3 Convs	**0.690**	**0.601**	0.419
Top-3 No Multi-Loss	0.633	0.524	0.338
Top-3 No 3D Pyramid	0.681	0.590	0.421
Top-5 Original U-Net	0.663	0.562	0.371

(a) Ensembles of Networks

2D-3D+3x3x3 (10.3M)	0.665	0.568	0.417
No 3x3x3 Convs (9.9M)	0.667	0.571	0.358
No Multi-Loss (10.3M)	0.652	0.550	0.355
No 3D Pyramid (7.9M)	0.646	0.542	0.376

(b) Single 2D-3D+3x3x3 Network and Ablations

Original U-Net (31.0M)	0.626	0.515	0.334
3D U-Net Thick (2.1M)	0.496	0.348	0.314
3D U-Net Thin (2.0M)	0.613	0.502	0.280
Deeplab + DRN (40.7M)	0.632	0.522	0.130
Deeplab + ResNet101 (59.3M)	0.585	0.456	0.124

(c) Baseline Networks

Table S1. Comprehensive network performance statistics. Segmentation algorithm results summary showing mean intersection-over-union (MIoU) across all classes (MIoU$^{(all)}$) on evaluation data and MIoU across organelle classes (MIoU$^{(org)}$) on evaluation and test data. The Subject 2 dataset from which the test data is taken contains only a small number of labeled cells among unlabeled ones; we use MIoU$^{(org)}$ to measure test performance since restricting the MIoU stat to labeled regions invalidates `background` and `cell` class statistics. (**a**) Results for the best ensemble from each architecture tested. A top-k ensemble averages the predictions of the best k trained networks as judged by MIoU$^{(all)}$ on the evaluation dataset. (**b**) Results for the best single network from each architecture class. Trainable parameter counts are in parentheses. (**c**) Results from baseline comparison networks. Trainable parameter counts are in parentheses